Film Formation Kinetics of Polymer Donor and Nonfullerene Acceptor Active Layers During Printing Out of 1,2,4-Trimethylbenzene in Ambient Conditions

Xinyu Jiang, Sebastian Grott, Volker Körstgens, Kerstin S. Wienhold, Zerui Li, Jinsheng Zhang, Christopher R. Everett, Matthias Schwartzkopf, Stephan V. Roth, and Peter Müller-Buschbaum*

Slot-die coating is a promising upscaling fabrication method to promote commercialization in the field of organic solar cells. Herein, the nonfullerene active layer blend of a conjugated polymer PffBT4T-2OD and a small molecule acceptor EH-IDTBR, which is printed out of the nonhalogenated solvent 1,2,4-trimethylbenzene, is studied. The film formation kinetics of the active layer PffBT4T-2OD:EH-IDTBR is probed in terms of the temporal evolutions in morphology as well as molecular conformation and aggregation as revealed by in situ grazing-incidence small angle X-ray scattering and UV–vis spectroscopy during the film printing process. A five-regime mesoscale domain growth process is observed in the active layer from the liquid state to the final dry state. The solvent evaporation-induced domain growth is accompanied with molecular stacking in a distinct J-type aggregation of the acceptor and a slight H-type aggregation of the donor molecules. The printed active layers exhibit an edge-on dominated PffBT4T-2OD and a face-on dominated EH-IDTBR crystallite structure. Compared to the neat PffBT4T-2OD and EH-IDTBR films, in the active layer, the crystallite structure deviates slightly in lattice spacing.

1. Introduction

In the past few decades, bulk heterojunction (BHJ) organic solar cells (OSCs) have gained significant improvements based on the developed novel materials and optimized fabrication routes.[1–8] For instance, due to the advantages of tunable molecular energy levels and light absorption of nonfullerene acceptors, the power conversion efficiency (PCE) of OSCs in a single junction device exceeded 19% and surpassed 20% in a tandem device geometry.[9–11] Typically, these high-performance OSCs are fabricated with the laboratory-scale spin-coating technique in a very limited device size and in an inert atmosphere. However, fabrication methods such as spin coating appear not well suitable for a large-scale real-world production of OSCs. Also, ambient conditions will be favorable over inert atmosphere conditions, which would increase production costs. To meet these requirements for the commercialization of OSCs, industrially large-scale, energy-saving, and low-cost fabrication techniques are desired.[12,13] Meniscus-guided slot-die coating, blade coating, and inkjet printing techniques have been proven to be excellent large-scale fabrication methods due to the large-area processing ability, simple operation process, low material consumption, and high-film homogeneity.[14–18] Meanwhile, OSC performance of over 17% PCE was realized with the slot-die coating method, which renders this method very promising in the commercialization of OSCs.[19] Although the PCE values of OSCs fabricated with two different methods start to become comparable, the film

X. Jiang, S. Grott, V. Körstgens, K. S. Wienhold, Z. Li, J. Zhang,
C. R. Everett, P. Müller-Buschbaum
Chair for Functional Materials
Department of Physics
TUM School of Natural Sciences
Technical University of Munich
James-Franck-Str. 1, 85748 Garching, Germany
E-mail: muellerb@ph.tum.de

M. Schwartzkopf, S. V. Roth
Deutsches Elektronen-Synchrotron DESY
Notkestraße 85, 22607 Hamburg, Germany

S. V. Roth
Department of Fibre and Polymer Technology
KTH Royal Institute of Technology
Teknikringen 56-58, SE-100 44 Stockholm, Sweden

P. Müller-Buschbaum
Heinz Maier-Leibnitz Zentrum (MLZ)
Technical University of Munich
Lichtenbergstr. 1, 85748 Garching, Germany

formation mechanisms are very different. The major difference between slot-die coating and spin coating is the duration of the solvent evaporation, which produces more far-from-equilibrium morphologies in spin-coated films. Furthermore, the spin coating process generates a centrifugal force that pulls the solution outward in the initial flow stages. Thus, knowledge about film formation during spin coating cannot be simply transferred to slot-die coating. At present, the focus in the large-scale fabrication of OSCs is to improve the PCE of printed devices through engineering of the slot-die coating parameters, such as temperature and atmosphere of the printing environment, print speed, etc.[20–23] However, the understanding of thin film formation kinetics as well as the donor–acceptor interaction during solvent evaporation is still under investigation. Some in situ studies have revealed the crystallinity and molecular conformation evolution in the active layer during the drying process. Nevertheless, the in-depth morphology formation is so far not fully understood due to the complexity of the processes.[24–27] Encouragingly, the advanced nondestructive grazing-incidence small-angle X-ray scattering (GISAXS) technique is capable of providing domain sizes and spatial correlations regarding the inner structures of films down to the nanometer scales, thereby allowing for the determination of the active layer morphology changes during the print process.[28–31]

In previous studies,[32–34] during printing, the temporal evolution of the morphology was analyzed for a few selected donor:acceptor blend systems only. For example, printing of active layers was studied and contained a conjugated low bandgap high-efficiency polymer donor named poly[(2,6-(4,8-bis(5-(2-ethylhexylthio)-4-fluorothiophen-2-yl)-benzo[1,2-b:4,5 b'] dithiophene)) -alt- (5,5-(1',3'-di-2-thienyl-5',7'-bis(2-ethylhexyl) benzo[1',2'-c:4',5' c'] dithiophene-4,8-dione)] (PBDB-T-SF) and the small molecule acceptor 3,9-bis (2 methylene-((3-(1,1-dicyanomethylene) −6,7-difluoro)-indanone)) −5,5,11,11-tetrakis (4 hexylphenyl)-dithieno [2,3-d:2',3'-d']-s-indaceno [1,2-b:5,6-b']dithiophene (IT-4F) as well as the donor poly[(2,6-(4,8-bis(5-(2-ethylhexyl-3-chloro)thiophen-2-yl) benzo [1,2-b:4,5-b']dithiophene))-alt-(5,5-(1',3'-di-2-thienyl-5',7'-bis(2 ethylhexyl) benzo [1',2'-c:4',5'-c'] dithiophene-4,8-dione)] (PBDB-T-2Cl) blended with the IT4F acceptor. In both cases, the printing was done out of chlorobenzene (CB) as solvent and the film formation kinetics were revealed by in situ GISAXS during printing. These pioneering studies demonstrated that the active layer formation kinetics and final morphology are highly dependent on the used materials, the host solvents, and the external conditions for the slot-die coating of the OSCs. In addition, when moving toward an industrial large-scale production of printed OSCs, halogen-based host solvents with high toxicity and carcinogenicity like chloroform (CF) and CB, will seriously limit their success. Recent studies from the OSC field with nonhalogenated solvents demonstrate that methylbenzenes such as toluene, xylene, and trimethylbenzene are very promising candidates due to the similar capabilities to their halogenated analogs, namely good solubility for a majority of oligomers and polymers in combination with environment-friendly characteristics.[35–37] Notably, 1,2,4-trimethylbenzene (TMB) is significantly more appropriate for commercialization since it is far less hazardous than other common nonhalogenated solvents (Table S1, Supporting Information). Thus, the utilization of a green nonhalogen-based host solvent coupled with the slot-die coating method and in-depth analysis of film formation kinetics are of great importance in the field of environment-friendly OSCs.[38,39]

In this study, the active layer containing the low bandgap donor polymer poly[(5,6-difluoro-2,1,3-benzothiadiazol-4,7-diyl)-alt-(3,3'''-di(2-octyldodecyl)-2,2';5',2'';5'',2'''-quaterthiophen-5,5'''-diyl)] (PffBT4T-2OD) and the nonfullerene acceptor (Z)-5-{[5-(15-{5-[(Z)-(3-ethyl-4-oxo-2-thioxo-1,3-thiazolidin-5-ylidene)methyl]-8-thia-7.9 diazabicyclo[4.3.0]nona-1(9),2,4,6-tetraen-2-yl]-9,9,18,18-tetrakis(2-ethylhexyl)-5.14 dithiapentacyclo[10.6.0.03,10.04,8.013,17]octadeca-1(12),2,4(8),6,10,13(17),15-heptaen-6-yl)-8-thia-7.9-diazabicyclo[4.3.0]nona-1(9),2,4,6-tetraen-2-yl]methylidene}-3-ethyl-2-thioxo-1,3-thiazolidin-4-one (EH-IDTBR) is printed out of the environment-friendly halogen-free solvent TMB at 60 °C with the slot-die coating method. The chemical structures of PffBT4T-2OD, EH-IDTBR, and TMB are given in **Figure 1**a. The combination of advantages such as being air-stable and thickness insensitive, together with a device performance of spin-coated PffBT4T-2OD:EH-IDTBR active layers over 9%, is essential for an interest in an industrial production of the related printed OSCs.[40–43] Furthermore, the high value of the lowest unoccupied molecular orbital (LUMO) energy level of the EH-IDTBR acceptor enables an excellent large open circuit voltage in OSC devices.[43] The evolution of active layer domains and the correlated changes in optical properties is revealed via in situ GISAXS and in situ UV–vis spectroscopy. The underlying effects of donor and acceptor on the active layer properties are seen in the in situ UV–vis measurements. Moreover, ex situ grazing-incidence wide-angle X-ray scattering (GIWAXS) measurements reveal information about the crystalline parts of the printed thin films. Thereby, this work gives insights into the morphology formation as well as the interactions between donor and acceptor in nonhalogen solvent-processed active layers during printing in ambient conditions.

2. Results and Discussion

2.1. Morphology Formation Kinetics

To give insights into the time evolution of the inner structure of active layers based on the donor:acceptor blend PffBT4T-2OD: EH-IDTBR during slot-die coating, we perform in situ GISAXS measurements. A sketch of the in situ GISAXS set-up is shown in Figure 1a, and selected 2D GISAXS data collected during the active layer formation is shown in Figure S1, Supporting Information. Horizontal line cuts of the 2D GISAXS data are performed at the Yoneda peak position of PffBT4T-2OD and EH-IDTBR to investigate characteristic lateral structures. The 2D color mapping of the horizontal line cuts is shown in Figure 1b over the progressive time of thin film drying. Figure 1c shows selected horizontal line cuts to demonstrate the kinetics of the inner structure formation. In more detail, the gradual increase in intensity in the high-q_y range reveals a growth of the small-size domains. Thereafter, the intensity further increases and shifts in the low-q_y range, suggesting growth of large domains.[44] To analyze the lateral structure evolution of the slot-die-coated PffBT4T-2OD:EH-IDTBR active layer in more depth during the film formation process, the data are modeled by assuming three cylindrical-shaped object types with different radii (large, middle, and small) to fit the horizontal line cut
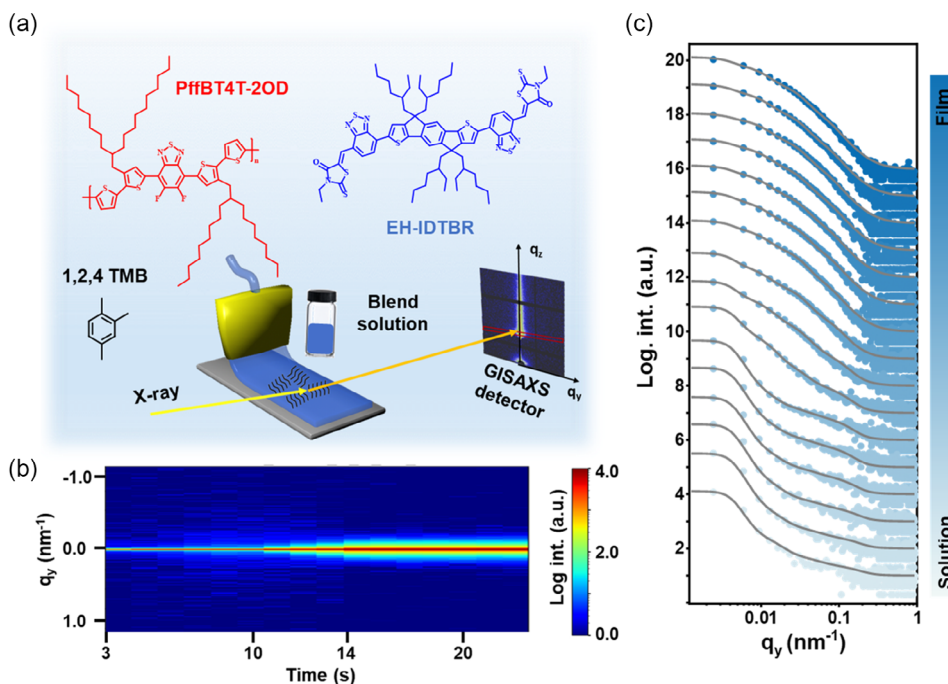
Figure 1. a) Chemical structures of the used materials (donor: PffBT4T-2OD, acceptor: EH-IDTBR, and solvent: TMB) and sketch of the in situ GISAXS measurement set-up. b) 2D color mapping of the temporal intensity evolution of horizontal line cuts of the 2D GISAXS data at the Yoneda peak position from in situ printing of PffBT4T-2OD:EH-IDTBR active layers out of TMB. c) Selected horizontal line cuts (blue dots) and respective fits (solid lines) for printed PffBT4T-2OD:EH-IDTBR active layers. The data are shifted along the y-axis from bottom to top for clarity and gradually plotted with darker color during the solvent evaporation to underline the transformation from solution to a dry film.

data.[45] To account for polydispersity of the domains, a Gaussian size distribution is assumed. The corresponding best fits to the data are shown in Figure 1c. The modeling is done in the framework of the distorted-wave Born approximation (DWBA) and the effective interface approximation (EIA).[46] With the experimental resolution of the in situ GISAXS experiment, domain sizes in the range of one to hundreds of nanometers are covered, which is well-suitable for understanding OSC active layers.

From the fit parameters, a domain size distribution is calculated to display the changes in characteristic lateral structures during printing of the active layer (**Figure 2**a). The individual fit parameters related to the small-, middle-, and large-sized domains such as domain radii, number of domains (intensity), and polydispersity (σ) are shown in Figure 2b–d, respectively. Similar to our previous reports on printing of donor:acceptor active layers,[32,47] five regimes are also distinguished in the film formation kinetics of the PffBT4T-2OD:EH-IDTBR active layer printed out of TMB as solvent. The initial regime (regime I) refers to the initial ink since the liquid solution is freshly deposited on the substrate and forms a liquid film. Obviously, aggregates have formed in the ink already, which have a constant size, number, and polydispersity. The observed domains have average radii of 7 ± 1 nm (small), 24 ± 4 nm (middle), and 81 ± 5 nm (large). Such preaggregation in the ink in the slot-die head was found before for other donor:acceptor blend solutions. In the second regime (regime II), a gradual and slow increase in all three domain radii is observed, while no obvious

changes in the domain numbers and the domain polydispersities are seen. Thus, parts of the domain solute start to interact as the solvent volatilizes from the printed film. The third regime (regime III) refers to the dramatic phase transition period due to the fast evaporation of the majority host solvent. There is an obvious domain size growth and an abrupt intensity increase reflecting the increase in domain numbers in all three types of domains. Interestingly, different from previous reports,[32,47] we observe an abrupt growth of the domains in the middle-size scale prior to the small-size scale. In addition to the original domain growth in the middle-size scale, this trend also might be caused by an additional aggregation of small-size domains. In the fourth regime (regime IV), as most parts of the solvent have evaporated, the solvent plays less of a role in the film formation of the active layer structure. We observe a decrease in domain radii for all three domain types accompanied by an increase in the corresponding domain numbers. In particular, a pronounced intensity growth of the small domain radii is observed rather than of the large and middle domain sizes. Moreover, there is an increase in the disorder of all three domain structures in regime four (Figure 2d). The very limited mobility in the late stages of film formation might cause more small and disordered features to form during this regime. In the last regime (regime V), the solvent is almost entirely evaporated. Thus, all parameters describing the domain structures in the active layer remain constant, thereby demonstrating an absence of mobility in the final PffBT4T-2OD:EH-IDTBR active layer.
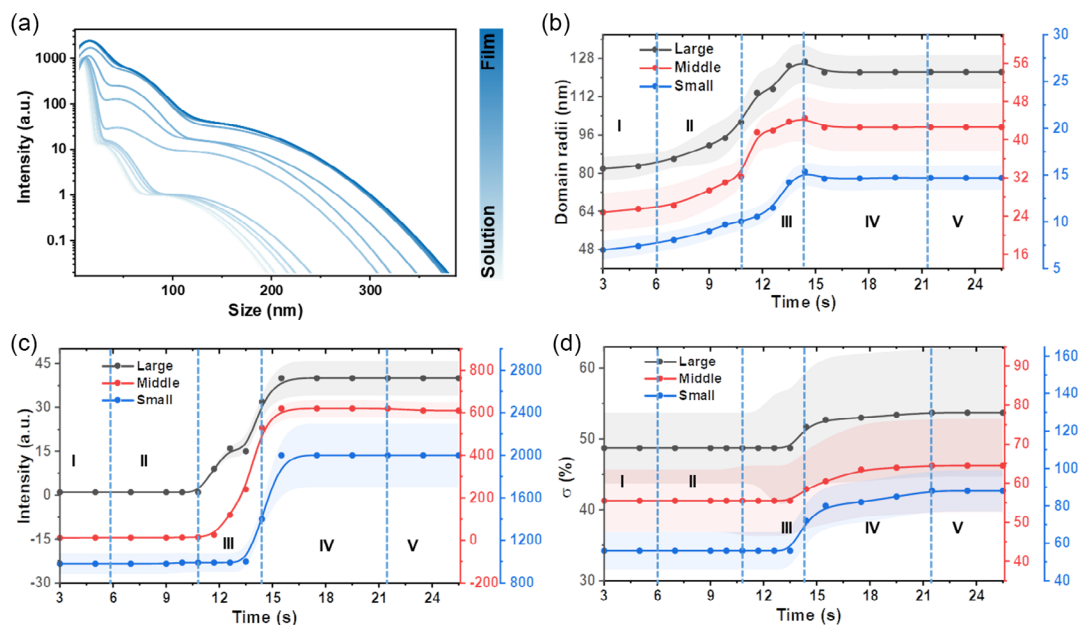
Figure 2. a) Temporal domain size evolution during the printing of PffBT4T-2OD:EH-IDTBR active layers out of TMB as determined from the GISAXS fits. The data are not normalized and gradually plotted with darker color during the solvent evaporation to underline the transformation from solution to a dry film. Temporal evolution of fit parameters describing the lateral film structure in terms of average domain b) radii, c) intensity, and d) polydispersity (σ) of the active layer. The solid lines act as guide to the eye and the shaded areas denote the error bar regimes. The vertical dashed lines mark the individual regimes *I–V*.

2.2. Molecular Conformation and Aggregation Kinetics

The evolution of the optical properties related to the conformation and aggregation kinetics of the PffBT4T-2OD:EH-IDTBR active layers printed out of TMB solvent as well as their neat thin films is studied in situ during printing with UV–vis spectroscopy.[48] The corresponding 2D color plots are shown in **Figure 3**a–c, and the detailed UV–vis spectroscopy is shown in Figure S2, Supporting Information. We observe clear differences in the drying behavior between the neat donor (Figure 3a), the neat acceptor (Figure 3b), and their blend films (Figure 3c). During the film formation process, the absorbance of the thin film clearly increases in the case of the neat PffBT4T-2OD thin film while it gradually decreases and redshifts in the case of the neat EH-IDTBR film. No obvious changes despite a redshift are seen for the PffBT4T-2OD:EH-IDTBR blend thin film. Due to an overlap in the absorption ranges of PffBT4T-2OD and EH-IDTBR, their temporal evolution cannot be easily traced in the absorbance data of the blend thin film. To identify the temporal molecular conformation and aggregation kinetics of PffBT4T-2OD and EH-IDTBR in the neat films and in the PffBT4T-2OD:EH-IDTBR blend film, a set of Gaussian functions with equal width that represents various optical transitions is utilized to fit the in situ UV–vis spectra.[49] Figure S3–S5, Supporting Information give the detailed fit information for these films. Six peaks located at 701.4, 658.5, 622.9, 583.8, 545.8, and 504.0 nm are assigned to the 0–0, 0–1, 0–2, 0–3, 0–4, 0–5, and 0–6 electronic transitions in PffBT4T-2OD. Three peaks at 632.8, 581.1, and 528.3 nm indicate the 0–0, 0–1, and 0–3 transitions in the neat EH-IDTBR. Thus, in total nine peaks with six

donor electronic transitions (from 0–0 to 0–6, at 701.9, 658.1, 624, 584, 546, and 503 nm) and three acceptor transitions (0–0, 0–1, and 0–2 at 632.3, 581.2, and 529 nm) are used for the PffBT4T-2OD:EH-IDTBR blend film (Figure S5, Supporting Information). In the final dried thin films, all electronic transitions broadened in both, neat and blend thin films, suggesting an increasing disorder.[50] The peak positions of donor and acceptor shift according to different trends in the neat and blend thin films during the film formation process.

To give insights into the interaction between donor and acceptor during the PffBT4T-2OD:EH-IDTBR blend film formation process, the temporal evolution of 0–0 electronic transitions is compared between neat donor and acceptor films and the blend film (Figure 3d–g). Matching the in situ GISAXS findings, five regimes are also seen in the in situ UV–vis data. However, in the details, the five different regimes differ from each other, in their temporal duration as well as in their processes. In the neat thin films, the intensity increases for PffBT4T-2OD but decreases for EH-IDTBR films in the initial regime (regime I), suggesting different aggregation behaviors between PffBT4T-2OD and EH-IDTBR. In the blend thin film, an intensity decrease is seen for EH-IDTBR while no changes happen for PffBT4T-2OD. In the second regime (regime II), the peak positions start to shift from their original positions, which is due to the aggregation of domain structures as observed in the GISAXS data analysis. The EH-IDTBR signal redshifts, while the PffBT4T-2OD signal blueshifts, indicating the J-type aggregation of the acceptor and a H-type aggregation of the donor molecules.[51,52] In the third regime (regime III), the trend of changes continues as in the second regime but with a much higher
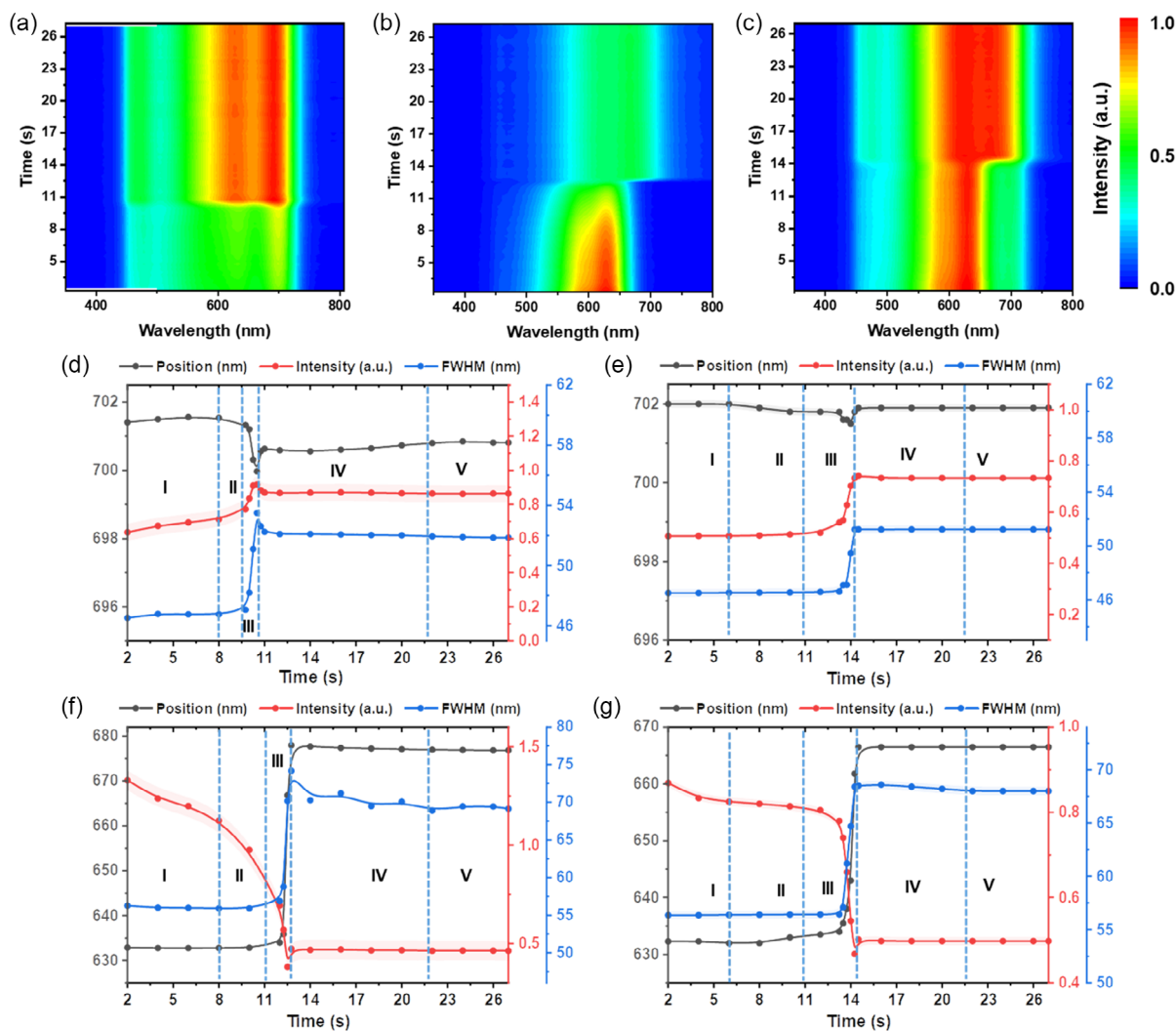
Figure 3. UV–vis data shown in a 2D color map during the film formation kinetics of a) neat PffBT4T-2OD, b) neat EHID-TBR, and c) PffBT4T-2OD:EH-IDTBR blend films printed out of TMB at 60 °C, respectively. Extracted 0–0 transition peak position (gray), peak intensity (red), and the corresponding FWHM (blue) of the polymer donor PffBT4T-2OD in d) neat films and e) PffBT4T-2OD:EH-IDTBR blend films as well as of the small molecular acceptor EH-IDTBR in f) neat films and g) blend films. The solid lines are guides to the eyes. The vertical dashed lines mark the individual regimes I–V.

strength, demonstrating a more intense aggregation of the EH-IDTBR and PffBT4T-2OD molecules. In addition, a rapid increase in the full width at half maximum (FWHM) values is observed, suggesting an increase in the disorder of the molecule packing. In the fourth regime (regime IV), a small but not negligible fallback of the peak positions, intensities, and the FWHM values is observed for the neat thin films. However, this phenomenon is insignificant in the blend thin film, especially in the PffBT4T-2OD signal, revealing the mutual influence on the formation of a donor–acceptor interaction during the drying. In the final regime (regime V), again all parameters are stable, suggesting the thin film is no more changing.

2.3. Crystal Structure

GIWAXS measurements are utilized to determine the crystallite structure of the final dried thin films.[53,54] **Figure 4**a and

Figure S6, Supporting Information demonstrate the 2D GIWAXS data of the neat PffBT4T-2OD film, neat EH-IDTBR film, and the PffBT4T-2OD:EH-IDTBR active layer, respectively.

The line profiles along the out-of-plane (OOP) and in-plane (IP) directions for the thin films are extracted from the 2D GIWAXS data with cake cuts (Figure 4b). The stacking distance of the crystallites is estimated by the Equation $d = 2\pi q^{-1}$, where q refers to the Bragg peak position. The neat donor polymer PffBT4T-2OD exhibits a very pronounced edge-on crystallite orientation along the substrate. The distinct main (100) Bragg peak, the (200) peak, and the (300) peak of PffBT4T-2OD are located at ≈ 0.28, ≈ 0.55, and ≈ 0.84 Å^{-1} in the OOP direction, respectively. Moreover, a weak (010) peak is located at ≈ 1.69 Å^{-1} in the IP direction, suggesting the excellent long-range ordering of PffBT4T-2OD crystallites in the neat polymer film. In contrast, the neat small molecule acceptor EH-IDTBR shows the opposite behavior. A (100) Bragg peak is located at ≈ 0.32 Å^{-1} in the IP
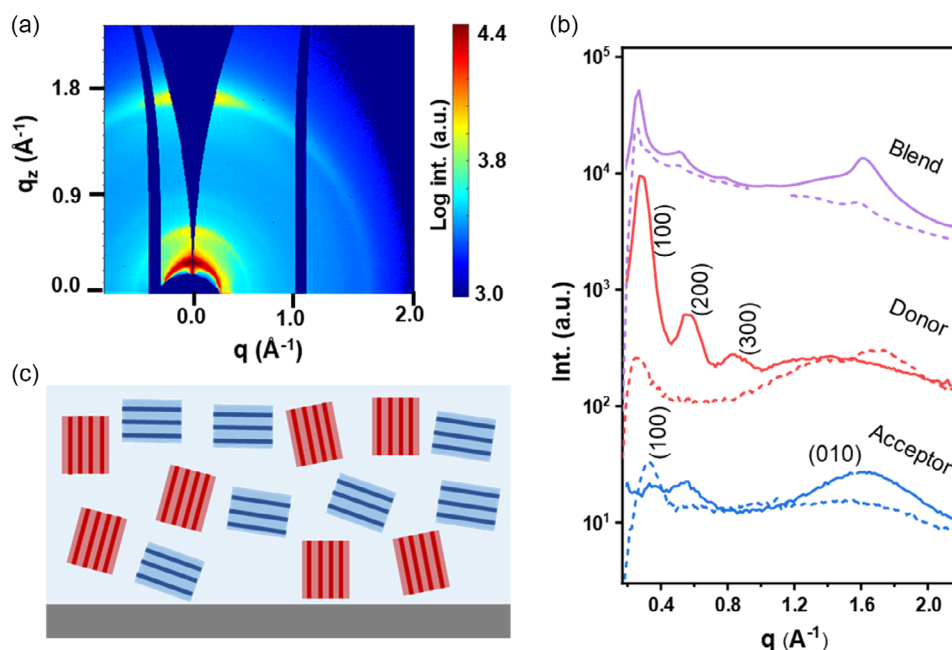
Figure 4. a) 2D GIWAXS data of PffBT4T-2OD:EH-IDTBR active layer printed out of TMB solvent. b) Out-of-plane (solid line) and in-plane (dash lines) profiles of the donor (PffBT4T-2OD), acceptor (EH-IDTBR), and blend (PffBT4T-2OD:EH-IDTBR) films, which are shifted along the y-axis for clarity. Characteristic Bragg peaks are indexed. c) Illustration of the crystalline orientation of the donor PffBT4T-2OD crystallites (red) and acceptor EH-IDTBR crystallites (blue) in the blend thin film, which is coated on the glass substrate (gray matrix).

direction and a (010) peak is located at $\approx 1.63\,\text{Å}^{-1}$ along the OOP direction, suggesting a typical face-on crystallite structure in the neat acceptor film. In the PffBT4T-2OD:EH-IDTBR blend thin film, both orientations are observed. Edge-on and face-on crystallites are present in the printed active layer, which are attributed to PffBT4T-2OD and EH-IDTBR, respectively (Figure 4c). The dominant edge-on (donor) and face-on (acceptor) orientations remain similar to the neat thin films. However, details of the crystalline structure show changes. Concerning the polymer donor, the (100), (200), and (300) Bragg peaks of PffBT4T-2OD move slightly toward lower values in the OOP direction, which are ≈ 0.27, ≈ 0.52, and $\approx 0.80\,\text{Å}^{-1}$. These changes demonstrate a larger lamellar stacking distance of PffBT4T-2OD in the blend thin film compared with the neat film. Concerning the small molecule acceptor, the (100) Bragg peak of EH-IDTBR moves to a higher q value $\approx 0.33\,\text{Å}^{-1}$ in the blend thin film, revealing a denser packing of the lamellar distance in the EH-IDTBR crystallites in the blend thin film compared with the neat film. Moreover, the (010) peak of EH-IDTBR decreases in its position to $\approx 1.61\,\text{Å}^{-1}$ along the OOP direction, which is attributed to the π–π stacking change of EH-IDTBR. Thus, we conclude that the face-on dominated EH-IDTBR crystallites in the blend thin films show a closer lamellar packing but a looser π–π stacking structure due to the presence of PffBT4T-2OD. The edge-on dominated PffBT4T-2OD crystallites are also perturbed by the presence of the small molecule acceptors. Thus, in total, the printed active layer is less perfect in its crystalline structure as compared to the neat films, which offers potential for a future optimization of the print process.

3. Conclusion

Toward the industrial large-scale production of OSCs, blend films of the nonfullerene small molecule acceptor EH-IDTBR and the polymer donor PffBT4T-2OD are printed out of a non-halogenated solvent using a slot-die coater. The utilizing ambient conditions with no need for an inert atmosphere and in combination with low-processing temperatures (60 °C), the blend system PffBT4T-2OD: EH-IDTBR is interesting for environmental-friendly upscaling. To gain a more detailed understanding of the complex film formation process during printing, the temporal evolution of the morphology and of the molecular conformation and aggregation properties is investigated by in situ GISAXS and in situ UV–vis measurements. A continuous growth process of the domain structures with five regimes is determined during the active layer printing. Notably, in the third regime, the most drastic growth happens for all domain sizes due to the fast evaporation of the solvent. In parallel, an abrupt molecular aggregation occurs in the acceptor as well as in the donor molecules, while the types of aggregates differ as differs the strength of the related 0–0 electronic transitions. Moreover, the abrupt growth of the domains in the middle-size scale prior to the small-size scale can be explained by the additional aggregation of small-size domains. After most of the solvent has evaporated, an increase in disorder across the domain structure is found. In the final dry active layer, the PffBT4T-2OD exhibits an edge-on crystal orientation while the EH-IDTBR has a face-on dominated crystallite structure along the substrate. Furthermore, the EH-IDTBR crystallites in the active layer show a denser lamellar packing but a looser π–π stacking structure, owing to the presence of

PffBT4T-2OD. In addition, the PffBT4T-2OD crystallites are perturbed by the presence of EH-IDTBR in the printed active layer. Notably, by a combination of the in situ and ex situ measurements, this work provides an in-depth study of the active layer formation kinetics while printing out of halogen-free solvent, which is of great importance in the commercialization of OSCs.

4. Experimental Section

Materials: The conjugated polymer donor poly[(5,6-difluoro-2,1,3-benzothiadiazol-4,7-diyl)-alt-(3,3′′′-di(2-octyldodecyl)-2,2′;5′,2′′;5′′,2′′′-quaterthiophene-5,5′′′-diyl)] (PffBT4T-2OD) and the small molecule acceptor (Z)-5-{[5-(15-{5-[(Z)-(3-Ethyl-4-oxo-2-thioxo-1,3-thiazolidin-5-ylidene)methyl]-8-thia-7,9-diazabicyclo[4.3.0]nona-1(9),2,4,6-tetraen-2-yl]-9,9,18,18-tetrakis(2-ethylhexyl)-5,14 dithiapentacyclo[10.6.0.03,10.04,8.013,17]octadeca-1(12),2,4(8),6,10,13(17),15-heptaen-6-yl]-8-thia-7,9-diazabicyclo[4.3.0]nona-1(9),2,4,6-tetraen-2-yl]methylidene}-3-ethyl-2-thioxo-1,3-thiazolidin-4-one (EH-IDTBR) were purchased from 1-Material Inc. The host solvent 1,2,4-trimethylbenzene (TMB) was obtained from Sigma–Aldrich and used as initially received without any further purification.

Thin Film Fabrication: The donor and acceptor were mixed in a 1:1 weight ratio and added into the TMB solution with a total concentration of $15 \, mg \, mL^{-1}$. The neat solutions of PffBT4T-2OD and EH-IDTBR were fabricated with a concentration of $8 \, mg \, mL^{-1}$ for the in situ UV–vis measurements, respectively. The solutions were stirred at least at 80 °C in a N_2 glovebox before printing. Glass slides with the size of $76 \times 26 \, mm^2$ were used as substrates and cleaned with an acid bath at 80 °C for 20 min. The acid bath solution ratio was $H_2SO_4{:}H_2O_2{:}H_2O = 54{:}84{:}198$. Subsequently, the substrates were rinsed with DI water to remove the acid residues and then dried with N_2 flow. A meniscus-guided slot-die coater with a constant print speed of $25 \, mm \, s^{-1}$ and solution flow rate of $0.2 \, mL \, min^{-1}$ was applied for thin film deposition. The substrates were heated to 60 °C during the printing at ambient conditions.

In Situ GISAXS Measurements: The in situ GISAXS measurements were performed at the beamline P03 at DESY in Hamburg with the X-ray wavelength of 0.96 Å (energy 12.9 keV).[55] The incident angle was set to 0.4° and the sample-to-detector distance (SDD) was 3,174 mm to obtain the active layer morphology evolution over time. A Pilatus 1 M detector with dimensions 981×1043 pixels (pixel size 172 µm $\times$ 172 µm) was used to collect the data. The direct beam reflected from the sample to the detector was shielded by a beamstop to protect the detector from oversaturation. The exposure time for each single GISAXS image was 0.1 s. The DPDAK software was used to obtain the transformation of detector image from pixel value to q-space and the horizontal line cuts at the Yoneda peak position.[56] The GISAXS fit software was used to perform further data analysis.

In Situ UV–vis Spectroscopy: In situ UV–vis spectrometer was mounted onto the slot-die coater. In more detail, an MBB1D1 broadband light emitting diode (THORLABS, Germany) was mounted as the light source below the sample holder. The emitting spectrum is given in Figure S7, Supporting Information. A spectrometer CAS 140 CT (Instrument Systems GmbH, Germany) located above the sample holder was used to record the transmission signal simultaneously in the range from 500 to 800 nm with a time resolution of 200 ms/spectrum. The light source and spectrometer were mounted vertically along the sample holder at a distance of 70 mm. The absorbance (A) values were calculated from the equation $A = -\lg(T)$, where T refers to the transmittance, which was calculated from the obtained signal.

GIWAXS Measurements: GIWAXS measurements were performed with a Ganesha SAXSLAB laboratory instrument with an X-ray wavelength of 1.54 Å for the neat films. The incident angle was 0.2° and the SDD was set to 95 mm. For the blend thin film, the measurement was performed at beamline P03 at DESY with the X-ray energy of 0.96 Å. The incident angle was 0.15° and the SDD was 180 mm. The GIWAXS signal was collected with a Pilatus 300 K detector with dimensions 487×619 pixels (pixel size 172 µm $\times$ 172 µm). The transformation to q-space and radial cuts for the in-plane/out-of-plane analysis were processed by the MATLAB-based package GIXSGUI.[57]

Supporting Information

Supporting Information is available from the Wiley Online Library or from the author.

Conflict of Interest

The authors declare no conflict of interest.

Data Availability Statement

The data that support the findings of this study are available from the corresponding author upon reasonable request.

[1] Z. Chen, X. Chen, Z. Jia, G. Zhou, J. Xu, Y. Wu, X. Xia, X. Li, X. Zhang, C. Deng, Y. Zhang, X. Lu, W. Liu, C. Zhang, Y. Yang, H. Zhu, *Joule* **2021**, *5*, 1832.

[2] Y. Firdaus, V. M. Le Corre, S. Karuthedath, W. Liu, A. Markina, W. Huang, S. Chattopadhyay, M. M. Nahid, M. I. Nugraha, Y. Lin, A. Seitkhan, A. Basu, W. Zhang, I. McCulloch, H. Ade, J. Labram, F. Laquai, D. Andrienko, L. J. A. Koster, T. D. Anthopoulos, *Nat. Commun.* **2020**, *11*, 5220.

[3] M. Zhang, L. Zhu, G. Zhou, T. Hao, C. Qiu, Z. Zhao, Q. Hu, B. W. Larson, H. Zhu, Z. Ma, Z. Tang, W. Feng, Y. Zhang, T. P. Russell, F. Liu, *Nat. Commun.* **2021**, *12*, 309.

[4] A. J. Gillett, A. Privitera, R. Dilmurat, A. Karki, D. Qian, A. Pershin, G. Londi, W. K. Myers, J. Lee, J. Yuan, S.-J. Ko, M. K. Riede, F. Gao, G. C. Bazan, A. Rao, T.-Q. Nguyen, D. Beljonne, R. H. Friend, *Nature* **2021**, *597*, 666.

[5] X. Song, L. Hou, R. Guo, Q. Wei, L. Yang, X. Jiang, S. Tu, A. Zhang, Z. Kan, W. Tang, G. Xing, P. Müller-Buschbaum, *ACS Appl. Mater. Interfaces* **2021**, *13*, 2961.

[6] K. S. Wienhold, X. Jiang, P. Müller-Buschbaum, *Appl. Phys. Lett.* **2020**, *116*, 120504.

[7] D. Yang, B. Cao, V. Körstgens, N. Saxena, N. Li, C. Bilko, S. Grott, W. Chen, X. Jiang, J. E. Heger, S. Bernstorff, P. Müller-Buschbaum, *ACS Appl. Energy Mater.* **2020**, *3*, 2604.

[8] X. Jiang, H. Kim, P. S. Deimel, W. Chen, W. Cao, D. Yang, S. Yin, R. Schaffrinna, F. Allegretti, J. V. Barth, M. Schwager, H. Tang, K. Wang, M. Schwartzkopf, S. V. Roth, P. Müller-Buschbaum, *J. Mater. Chem. A* **2020**, *8*, 23628.

[9] L. Zhu, M. Zhang, J. Xu, C. Li, J. Yan, G. Zhou, W. Zhong, T. Hao, J. Song, X. Xue, Z. Zhou, R. Zeng, H. Zhu, C.-C. Chen, R. C. I. MacKenzie, Y. Zou, J. Nelson, Y. Zhang, Y. Sun, F. Liu, *Nat. Mater.* **2022**, *21*, 656.

[10] Z. Zheng, J. Wang, P. Bi, J. Ren, Y. Wang, Y. Yang, X. Liu, S. Zhang, J. Hou, *Joule* **2022**, *6*, 171.

[11] W. Gao, F. Qi, Z. Peng, F. R. Lin, K. Jiang, C. Zhong, W. Kaminsky, Z. Guan, C.-S. Lee, T. J. Marks, H. Ade, A. K.-Y. Jen, *Adv. Mater.* **2022**, *34*, 2202089.

[12] R. Xue, J. Zhang, Y. Li, Y. Li, *Small* **2018**, *14*, 1801793.

[13] M. Riede, D. Spoltore, K. Leo, *Adv. Energy Mater.* **2021**, *11*, 2002653.

[14] D. Lohse, *Annu. Rev. Fluid Mech.* **2022**, *54*, 349.

[15] X. Ding, J. Liu, T. A. L. Harris, *AIChE J.* **2016**, *62*, 2508.

[16] Y. Xiao, C. Zuo, J.-X. Zhong, W.-Q. Wu, L. Shen, L. Ding, *Adv. Energy Mater.* **2021**, *11*, 2100378.

[17] X. Jiang, P. Chotard, K. Luo, F. Eckmann, S. Tu, M. A. Reus, S. Yin, J. Reitenbach, C. L. Weindl, M. Schwartzkopf, S. V. Roth, P. Müller-Buschbaum, *Adv. Energy Mater.* **2022**, *12*, 2103977.

[18] J. Yuan, D. Liu, H. Zhao, B. Lin, X. Zhou, H. B. Naveed, C. Zhao, K. Zhou, Z. Tang, F. Chen, W. Ma, *Adv. Energy Mater.* **2021**, *11*, 2100098.

[19] J. Xue, H. Zhao, B. Lin, Y. Wang, Q. Zhu, G. Lu, B. Wu, Z. Bi, X. Zhou, C. Zhao, G. Lu, K. Zhou, W. Ma, *Adv. Mater.* **2022**, *34*, 2202659.

[20] L. X. Chen, *ACS Energy Lett.* **2019**, *4*, 2537.

[21] N. Han, Y.-J. Heo, M. Lee, Y. Moon, D. Yang, Y. Kim, D.-Y. Kim, *Adv. Funct. Mater.* **2022**, *32*, 2204871.

[22] J. Lee, Y.-H. Seo, S.-N. Kwon, D.-H. Kim, S. Jang, H. Jung, Y. Lee, H. Weerasinghe, T. Kim, J. Y. Kim, D. Vak, S.-I. Na, *Adv. Energy Mater.* **2019**, *9*, 1901805.

[23] S. Song, K. T. Lee, C. W. Koh, H. Shin, M. Gao, H. Y. Woo, D. Vak, J. Y. Kim, *Energy Environ. Sci.* **2018**, *11*, 3248.

[24] R. Ma, C. Yan, P. W.-K. Fong, J. Yu, H. Liu, J. Yin, J. Huang, X. Lu, H. Yan, G. Li, *Energy Environ. Sci.* **2022**, *15*, 2479.

[25] B. Schmidt-Hansberg, M. F. G. Klein, K. Peters, F. Buss, J. Pfeifer, S. Walheim, A. Colsmann, U. Lemmer, P. Scharfer, W. Schabel, *J. Appl. Phys.* **2009**, *106*, 124501.

[26] W. Zhong, Q. Hu, Y. Jiang, Y. Li, T. L. Chen, L. Ying, F. Liu, C. Wang, Y. Liu, F. Huang, Y. Cao, T. P. Russell, *Sol. RRL* **2019**, *3*, 1900032.

[27] M. Abdelsamie, N. D. Treat, K. Zhao, C. McDowell, M. A. Burgers, R. Li, D.-M. Smilgies, N. Stingelin, G. C. Bazan, A. Amassian, *Adv. Mater.* **2015**, *27*, 7285.

[28] P. Müller-Buschbaum, *Adv. Mater.* **2014**, *26*, 7692.

[29] D. Moseguí González, C. J. Schaffer, S. Pröller, J. Schlipf, L. Song, S. Bernstorff, E. M. Herzig, P. Müller-Buschbaum, *ACS Appl. Mater. Interfaces* **2017**, *9*, 3282.

[30] A. Mahmood, J.-L. Wang, *Sol. RRL* **2020**, *4*, 2000337.

[31] S. Pröller, F. Liu, C. Zhu, C. Wang, T. P. Russell, A. Hexemer, P. Müller-Buschbaum, E. M. Herzig, *Adv. Energy Mater.* **2016**, *6*, 1501580.

[32] K. S. Wienhold, V. Körstgens, S. Grott, X. Jiang, M. Schwartzkopf, S. V. Roth, P. Müller-Buschbaum, *Sol. RRL* **2020**, *4*, 2000086.

[33] K. S. Wienhold, C. L. Weindl, S. Yin, T. Tian, M. Schwartzkopf, A. Rothkirch, S. V. Roth, P. Müller-Buschbaum, *ACS Appl. Mater. Interfaces* **2020**, *12*, 40381.

[34] K. Vegso, P. Siffalovic, M. Jergel, P. Nadazdy, V. Nadazdy, E. Majkova, *ACS Appl. Mater. Interfaces* **2017**, *9*, 8241.

[35] C.-C. Chueh, K. Yao, H.-L. Yip, C.-Y. Chang, Y.-X. Xu, K.-S. Chen, C.-Z. Li, P. Liu, F. Huang, Y. Chen, W.-C. Chen, A. K.-Y. Jen, *Energy Environ. Sci.* **2013**, *6*, 3241.

[36] H. Bouzid, M. Prosa, M. Bolognesi, N. Chehata, D. Gedefaw, C. Albonetti, M. R. Andersson, A. Muccini, A. Bouazizi, M. Seri, *J. Polym. Sci., Part A: Polym. Chem.* **2019**, *57*, 487.

[37] C.-H. Zhang, F. Lin, W. Huang, J. Xin, J. Wang, Z. Lin, W. Ma, T. Yang, J. Xia, Y. Liang, *J. Mater. Chem. C* **2020**, *8*, 11532.

[38] S. Hultmark, S. H. K. Paleti, A. Harillo, S. Marina, F. A. A. Nugroho, Y. Liu, L. K. E. Ericsson, R. Li, J. Martín, J. Bergqvist, C. Langhammer, F. Zhang, L. Yu, M. Campoy-Quiles, E. Moons, D. Baran, C. Müller, *Adv. Funct. Mater.* **2020**, *30*, 2005462.

[39] L. Hong, H. Yao, Z. Wu, Y. Cui, T. Zhang, Y. Xu, R. Yu, Q. Liao, B. Gao, K. Xian, H. Y. Woo, Z. Ge, J. Hou, *Adv. Mater.* **2019**, *31*, 1903441.

[40] A. J. Clarke, J. Luke, R. Meitzner, J. Wu, Y. Wang, H. K. H. Lee, E. M. Speller, H. Bristow, H. Cha, M. J. Newman, K. Hooper, A. Evans, F. Gao, H. Hoppe, I. McCulloch, U. S. Schubert, T. M. Watson, J. R. Durrant, W. C. Tsoi, J.-S. Kim, Z. Li, *Cell Rep. Phys. Sci.* **2021**, *2*, 100498.

[41] N. Gasparini, A. Wadsworth, M. Moser, D. Baran, I. McCulloch, C. J. Brabec, *Adv. Energy Mater.* **2018**, *8*, 1703298.

[42] G. Zhang, R. Xia, Z. Chen, J. Xiao, X. Zhao, S. Liu, H.-L. Yip, Y. Cao, *Adv. Energy Mater.* **2018**, *8*, 1801609.

[43] H. Cha, J. Wu, A. Wadsworth, J. Nagitta, S. Limbu, S. Pont, Z. Li, J. Searle, M. F. Wyatt, D. Baran, J.-S. Kim, I. McCulloch, J. R. Durrant, *Adv. Mater.* **2017**, *29*, 1701156.

[44] M. Schwartzkopf, A. Buffet, V. Körstgens, E. Metwalli, K. Schlage, G. Benecke, J. Perlich, M. Rawolle, A. Rothkirch, B. Heidmann, G. Herzog, P. Müller-Buschbaum, R. Röhlsberger, R. Gehrke, N. Stribeck, S. V. Roth, *Nanoscale* **2013**, *5*, 5053.

[45] S. Guo, W. Wang, E. M. Herzig, A. Naumann, G. Tainter, J. Perlich, P. Müller-Buschbaum, *ACS Appl. Mater. Interfaces* **2017**, *9*, 3740.

[46] A. L. Oechsle, J. E. Heger, N. Li, S. Yin, S. Bernstorff, P. Müller-Buschbaum, *ACS Appl. Mater. Interfaces* **2022**, *14*, 30802.

[47] D. Yang, S. Grott, X. Jiang, K. S. Wienhold, M. Schwartzkopf, S. V. Roth, P. Müller-Buschbaum, *Small Methods* **2020**, *4*, 2000418.

[48] M. Abdelsamie, K. Zhao, M. R. Niazi, K. W. Chou, A. Amassian, *J. Mater. Chem. C* **2014**, *2*, 3373.

[49] S. T. Hoffmann, H. Bässler, A. Köhler, *J. Phys. Chem. B* **2010**, *114*, 17037.

[50] A. W. Götz, J. I. Rodríguez, F. L. Castillo-Alvarado, D. E. Trujillo-González, *Int. J. Quantum Chem.* **2019**, *119*, e25883.

[51] F. C. Spano, C. Silva, *Annu. Rev. Phys. Chem.* **2014**, *65*, 477.

[52] F. C. Spano, *Acc. Chem. Res.* **2010**, *43*, 429.

[53] Y.-W. Su, Y.-C. Lin, K-H. Wei, *J. Mater. Chem. A* **2017**, *5*, 24051.

[54] H. Lee, D. Lee, D. H. Sin, S. W. Kim, M. S. Jeong, K. Cho, *NPG Asia Mater.* **2018**, *10*, 469.

[55] A. Buffet, A. Rothkirch, R. Döhrmann, V. Körstgens, M. M. Abul Kashem, J. Perlich, G. Herzog, M. Schwartzkopf, R. Gehrke, P. Müller-Buschbaum, S. V. Roth, *J. Synchrotron Rad.* **2012**, *19*, 647.

[56] G. Benecke, W. Wagermaier, C. Li, M. Schwartzkopf, G. Flucke, R. Hoerth, I. Zizak, M. Burghammer, E. Metwalli, P. Müller-Buschbaum, M. Trebbin, S. Förster, O. Paris, S. V. Roth, P. Fratzl, *J. Appl. Cryst.* **2014**, *47*, 1797.

[57] Z. Jiang, *J. Appl. Cryst.* **2015**, *48*, 917.